

High-temperature deformation behaviour of as-cast $\text{Al}_{0.4}\text{Co}_{0.9}\text{Cr}_{1.2}\text{Fe}_{0.9}\text{Ni}_{1.2}(\text{Si}, \text{Ti}, \text{C}, \text{B})_{0.375}$ complex concentrated alloy during tensile and compression tests

Michaela Štamborská*, Tatiana Pelachová

*Institute of Materials and Machine Mechanics, Slovak Academy of Sciences,
Dúbravská cesta 9, 845 13 Bratislava, Slovak Republic*

Received 19 August 2023, received in revised form 2 October 2023, accepted 4 October 2023

Abstract

The deformation behaviour of as-cast $\text{Al}_{0.4}\text{Co}_{0.9}\text{Cr}_{1.2}\text{Fe}_{0.9}\text{Ni}_{1.2}(\text{Si}, \text{Ti}, \text{C}, \text{B})_{0.375}$ complex concentrated alloy (CCA) in the temperature range from 700 up to 900 °C during tensile and compression tests was studied. The as-cast alloy was prepared by vacuum induction melting in a ceramic crucible followed by a tilt casting to a graphite mould. Highly anisotropic microstructure of tensile and compression specimens taken from the as-cast ingot consisted of 89 vol.% of columnar FCC(A1) (face-centred cubic crystal structure A1) dendrites and 11 vol.% of the multiphase interdendritic region where ordered phases as Cr_2B , TiC, BCC(B2) (ordered body-centred cubic crystal structure B2) + BCC(A2) (disordered body-centred cubic crystal structure A2), and lamellar eutectic composed of FCC(A1) + G – $(\text{Ni}, \text{Co}, \text{Fe})_{16}(\text{Ti}, \text{Cr})_6(\text{Si}, \text{Al})_7$ (cubic face-centred crystal structure) phase were formed during solidification. Columnar FCC(A1) dendrite grains were oriented at an angle ranging from 60° to 90° to the longitudinal axis of the test specimens.

The value of 0.2 % offset yield strength decreases with increasing applied temperature, at 700 °C tension and compression, it was measured to be about (429 ± 3) MPa and at 900 °C it decreased to the value of about (90 ± 5) MPa. The alloy during tensile deformation at 700 °C shows the strain hardening stage up to fracture. The tensile deformation true strain-true stress curves at 800 °C and compression deformation true strain-true stress curves at temperatures from 700 to 800 °C show the strain hardening stage at initial strains. After reaching the peak values, the strain softening stage is typical for the alloy. The strain softening stage results from partial dynamic recrystallisation of FCC(A1) dendrites and fracture of brittle high elastic modulus phases in the interdendritic region. The compression and tensile curves at the temperature of 900 °C show a short area of the strain hardening stage, followed by a steady-state deformation at a constant flow stress. The finite element analysis (FEA) of the 3D distribution of local equivalent strains corresponds qualitatively to the observed structural changes within the necked and barrelled specimens.

Key words: complex concentrated alloys, microstructure, numerical modelling, mechanical properties, fracture

1. Introduction

For more than a decade, scientists have devoted their interest to a new class of materials called high-entropy alloys (HEAs) and related concepts (multiple principal element alloys – MPEAs and complex concentrated alloys – CCAs) [1–10]. HEAs composed of five or more principal elements of equal or nearly equal

composition form single-phase disordered solid solutions, such as face-centred cubic (FCC), body-centred cubic (BCC) or hexagonal close-packed (HCP), due to the high entropy of mixing of the solution elements [1, 3]. Concept of CCAs focused on more compositional variations farther from the equal composition offers new opportunities in microstructure and property design including formation of ordered phases

*Corresponding author: e-mail address: michaela.stamborska@savba.sk

[2, 8–14]. Among numerous studied HEA/CCA alloys, $\text{Al}_x\text{CoCrFeNi}$ alloys (x is a molar ratio) where $0.1 < x < 3$, attracted a large interest since in dependence of Al content and used processing routes, different variations of microstructure and mechanical properties can be achieved [15–30]. For $x < 0.5$, these alloys contain a single FCC(A1) (face-centred cubic crystal structure A1) phase; for $0.5 \leq x < 0.9$, their microstructure consists of a mixture of FCC(A1) and BCC(B2) (ordered body-centred cubic crystal structure B2) phases, which changes to a mixture of ordered BCC(B2) and disordered BCC(A2) (body-centred cubic crystal structure A2) phases for $0.9 \leq x \leq 2$ [17–21]. The CCA concept enables the formation of ordered phases in HEA alloys by minor additions of Ti, C, B, Mn, Cu, and Si [31–51]. These small additions are often effective in forming L_{12} , σ or BCC(B2) precipitates in the FCC matrix with a strong hardening effect [15, 19]. Moreover, depending on the amount and combination of different additions, brittle ordered phases like TiC or Cr_2B can be formed in CCAs during casting [27, 35, 36, 47, 48], which could be detrimental to the mechanical properties.

The effect of the cooling rate, grain size, alloying variations, thermo-mechanical processing, annealing or strain rate at room and higher temperatures on compressive or tensile properties in the $\text{Al}_{(0.1-0.5)}\text{CoCrFeNi}$ alloys were explored by many researchers [16–18, 20, 25–44]. A lot of them deal with properties of CCAs with FCC(A1) or (FCC(A1) + BCC(A2) structure affected by the formation of ordered multiphase structures [11, 13, 31, 32, 34–41, 47, 48, 50].

Only limited attention was paid to the deformation behaviour of HEA/CCAs during both tensile and compressive loading [51–53]. Deformation within the tested specimens is connected with local plastic instabilities – a necking in tension [54–56] and barrelling in compression [31, 48, 57]. These local plastic instabilities depend not only on intrinsic material properties but specimen geometry as well. Compression tests are widely used to understand the deformation behaviour of various materials at elevated temperatures [31, 48, 57]. The strain inhomogeneity in the compression specimen, which results in barrelling causing a triaxial stress state during deformation, arises due to intrinsic material properties and friction at the interfaces between the compression specimen and the platens [31].

The present article aims to study the deformation behaviour of as-cast multiphase $\text{Al}_{0.4}\text{Co}_{0.9}\text{Cr}_{1.2}\text{Fe}_{0.9}\text{Ni}_{1.2}(\text{Si}, \text{Ti}, \text{C}, \text{B})_{0.375}$ alloy during tension and compression tests. The finite element analysis (FEA) is applied for 3D numerical modelling of equivalent strains within necked tension and barrelled compression specimens at temperatures of 700 °C, 800 °C, and 900 °C.

2. Experimental materials and methods

2.1. Material preparation

The vacuum induction melting (VIM) was used to prepare the studied alloy with a nominal composition of $\text{Al}_{0.4}\text{Co}_{0.9}\text{Cr}_{1.2}\text{Fe}_{0.9}\text{Ni}_{1.2}(\text{Si}, \text{Ti}, \text{C}, \text{B})_{0.375}$. The charge consisted of master Ni-19Al-8Cr-5Ti-3B (in at.%) alloy and pieces of pure Al, Cr, Fe, and Co (purity better than 99.95 %). The VIM of the charge was realised in a ceramic crucible composed of 68 % SiO_2 + 18 % SiC + 14 % Al_2O_3 with an inside diameter of 80 mm and a height of 250 mm. Due to the thermo-chemical reactions between the melt and used crucible/mould, the alloy was contaminated by additions of Si and C. The vacuum chamber of the induction furnace LINN-IT-KTV 20/1.5 was evacuated to a vacuum pressure of 4.8 Pa, flushed with argon three times, and finally partially filled with argon (purity of 99.9995 %) to a vacuum pressure of 10 kPa to minimise evaporation loss of Al during melting. The melt temperature of 1600 °C and hold time of 10 min were used to dissolve all alloying elements of the charge fully. A pyrometer monitored the temperature of the melt. The alloy was tilt-cast into a cold graphite mould. An as-cast ingot with a diameter of 38 mm and length of 225 mm was cut into cylindrical bars for mechanical testing by wire electrical discharge machining. The cylindrical bars had a diameter of 8.5 mm and a length of 55 mm.

2.2. Microstructure evaluation

The microstructure of the alloy was studied by scanning electron microscopy (SEM) in back-scattered electron (BSE) mode using a JEOL 7600 F microscope equipped with an energy-dispersive X-ray spectrometer (EDS). The samples for microstructure observation were prepared by standard metallographic techniques, including grinding on SiC papers and polishing using diamond suspensions up to 0.3 μm particle size. The average content of carbon in the as-cast alloy was measured by LECO CS844 elemental analyser.

2.3. Mechanical testing

Cylindrical tensile specimens with threaded heads were prepared by lathe machining. The gauge diameter of the specimens was 5 mm, and the gauge length was 25 mm. In order to remove the stress concentrators, the surface of the gauge section of the tensile samples was polished to a roughness better than 0.3 mm using diamond paste. The universal testing machine Zwick/Roell Z100 was used for tensile testing at temperatures 700, 800, and 900 °C at an initial strain rate of $1 \times 10^{-4} \text{ s}^{-1}$. 5–6 specimens for each tensile test regime were used. The test temperature of



Fig. 1. Finite element mesh applied for the (a) cylindrical tensile and (b) compression specimens.

the specimens was reached in the resistance furnace at a heating rate of $10^{\circ}\text{C min}^{-1}$ and maintained at the test temperature for 30 min before the tensile test. K-type thermocouple touching the gauge section of the specimens monitored the temperature during the test. The high-temperature extensometer MAYTEC PMA-12/V7 with ceramic sensor arms was used to measure the elongation on the surface of specimens.

Cylindrical compression specimens (3 specimens for each test temperature) with a diameter of 6 mm and a length of 9 mm were prepared by lathe machining and finalised by polishing to a roughness better than $0.3\ \mu\text{m}$ using a diamond paste. The compression specimens were deformed at an initial strain rate of $1 \times 10^{-4}\ \text{s}^{-1}$ to engineering strains of 0.4 using a Gleeble 3800 thermomechanical tester at temperatures 700, 800, and 900°C .

2.4. Numerical modelling

The strain fields were determined by finite element analysis (FEA) software *Ansys Workbench*. A geometry model of the tensile specimens was built as a 3D cylindrical specimen with a gauge diameter of 5 mm. The material model was built using the experimental data obtained from the tensile tests. The input data required for the elastic-plastic model in FEA, such as Young's modulus, Poisson's ratio, true stress, true plastic strain, and strain hardening curve, were determined experimentally by the tensile tests, and for the softening part, Drucker-Prager softening linear model of the studied material was calculated. For 3D analysis, deformable tetrahedron elements with a size of 0.5 mm were used to mesh the cylindrical tensile specimen (Fig. 1a). In total, the mesh was composed of 26,991 tetrahedron elements, adding up to 47,850 nodes in total. Numerical calculations were realised for tensile specimens tested to the fracture.

A geometry model of the compression specimens was built as a 3D cylinder with a diameter of 6 mm and a height of 9 mm. Two compressive plates were

modelled as 3D plates. Triaxial stress distribution was assumed to occur due to friction between the platens and specimen with a friction coefficient of 0.1 [57], and 3D analysis was used instead of an axisymmetric one. The material model was built using the experimental data from the compression tests. The input data required for the elastic-plastic model in FEA, such as Young's modulus, Poisson's ratio, true stress, true plastic strain, and strain hardening curve, were determined experimentally by the compression tests, and for the softening part, Drucker-Prager softening linear model of the studied material was calculated. For 3D analysis, deformable hexahedron elements with a size of 0.2 and 0.5 mm were used to mesh the cylindrical specimen and platens, respectively, as shown in Fig. 1b. In total, the mesh was composed of 65,464 hexahedral elements, adding up to 274,067 nodes. Numerical calculations were carried out for specimens tested up to true strain of 0.51.

3. Results and discussion

3.1. Initial microstructure of the test samples

Figure 2a shows the microstructure of the longitudinal section of cylindrical bars cut from the as-cast ingot of the alloy with a nominal composition $\text{Al}_{0.4}\text{Co}_{0.9}\text{Cr}_{1.2}\text{Fe}_{0.9}\text{Ni}_{1.2}(\text{Si}, \text{Ti}, \text{C}, \text{B})_{0.375}$ which were used for the fabrication of tensile and compression specimens. An arrow indicates the load direction during mechanical tests. The microstructure consists of columnar dendrites (D) and multiphase interdendritic region (IR). FCC(A1) dendrites follow $\langle 001 \rangle$ crystallographic orientation close to the heat flux direction during the solidification of the alloy [47]. Taking the $\langle 001 \rangle$ crystallographic direction of the FCC(A1) dendrites, adjacent grains are rotated to each other by a small angle and inclined to the load axis under the angle of 60° – 84° . Only within a few grains is the crystallographic direction of the dendrites oriented par-

Table 1. Chemical composition of studied and comparative alloys and areas of FCC(A1) dendrites (at.%)

Alloy/Area	Al	Co	Cr	Fe	Ni	Si	Ti	C	B	Ref.
Studied alloy	8±0.3	18.3±0.3	24.3±0.3	18.1±0.1	23.7±0.3	4±0.1	2.1±0.1	0.5±0.1	1±0.1	–
FCC(A1) dendrites in the studied alloy	7.3±0.5	19.6±0.1	24.4±0.1	19.8±0.5	24.3±0.6	3.6±0.6	1±0.2	–	–	–
FCC(A1) dendrites in Al _{0.5} CoCr _{1.3} FeNi _{1.3} (Ti, Si, B, C) _{0.3} alloy	8.2±1.1	19.6±0.6	24.0±0.6	19.7±0.3	24.7±0.3	2.2±0.7	1.6±0.5	–	–	47
Al _{0.3} CoCrFeNi alloy	6.98±0.2	23.25±0.1	23.89±0.1	23.25±0.1	22.6±0.4	–	–	–	–	43

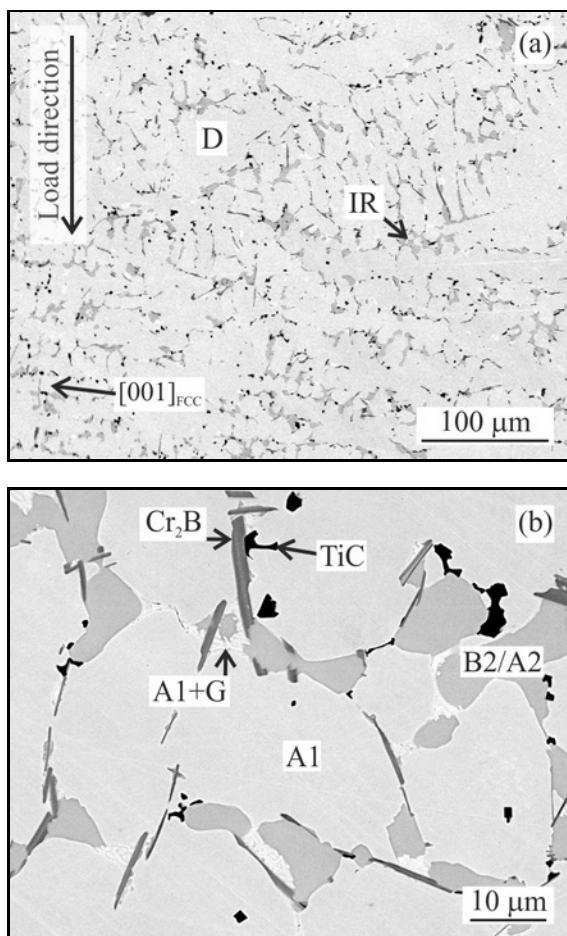


Fig. 2. The microstructure of cylindrical bars cut from the as-cast ingot: (a) BSE micrograph showing grain boundaries with columnar dendrite (D) morphology and (b) BSE micrograph showing the morphology of coexisting phases formed in the vicinity of the dendrite/interdendritic region (IR).

allel to the load axis in the test samples. FCC(A1) dendrites are enriched in Co and Fe and depleted in Al and Ni compared to the interdendritic area [48].

Table 1 shows the measured chemical composition of the studied alloy and FCC(A1) dendrites. Figure 2b shows the multiphase interdendritic region where several coexisting phases/areas were formed. Plate-like particles belong to the Cr₂B phase. A two-phase microstructure consisting of the ordered BCC(B2) phase with very fine cuboidal-shaped precipitates of disordered BCC(A2) phase is formed in their close vicinity. Lamellar eutectic areas composed of FCC(A1) and G – (Ni,Co,Fe)₁₆(Ti,Cr)₆(Si,Al)₇ phases are observed in the interdendritic region [48]. Black irregularly shaped particles belong to the TiC phase. The as-cast microstructure of the studied alloy is described in more detail in our article [48].

3.2. Tensile and compression curves

Figures 3a–c show the experimental tensile and compression engineering stress-strain curves for the specimens tested at temperatures of 700, 800, and 900 °C, respectively. All samples were tested at an initial strain rate of $1 \times 10^{-4} \text{ s}^{-1}$. Tensile tests were carried out until the fracture; compression tests were carried out up to the engineering strain of 0.4. The studied alloy shows plastic behaviour during all tested regimes, which is strongly dependent on the applied temperature. Tensile yield strength drops by 80 %, and elongation increases by 258 % with increasing test temperature from 700 to 900 °C.

Figure 3d shows the temperature dependence of average 0.2 % offset tensile (YS_T) and compression (YS_C) yield strength. Both YS_T and YS_C decrease with the increasing test temperature. The same temperature dependence of YS was found for many HEA/CCA alloys with FCC(A1) structure [16, 47, 48, 51]. While 700 and 900 °C values of YS_T and YS_C are very close, a higher value of YS_C of about 14 % compared to YS_T was observed at 800 °C tests. The averaged value of YS = (429 ± 3) MPa measured at 700 °C decreased to the value of (90 ± 5) MPa with increasing the temperature to 900 °C. The high-temperature ten-

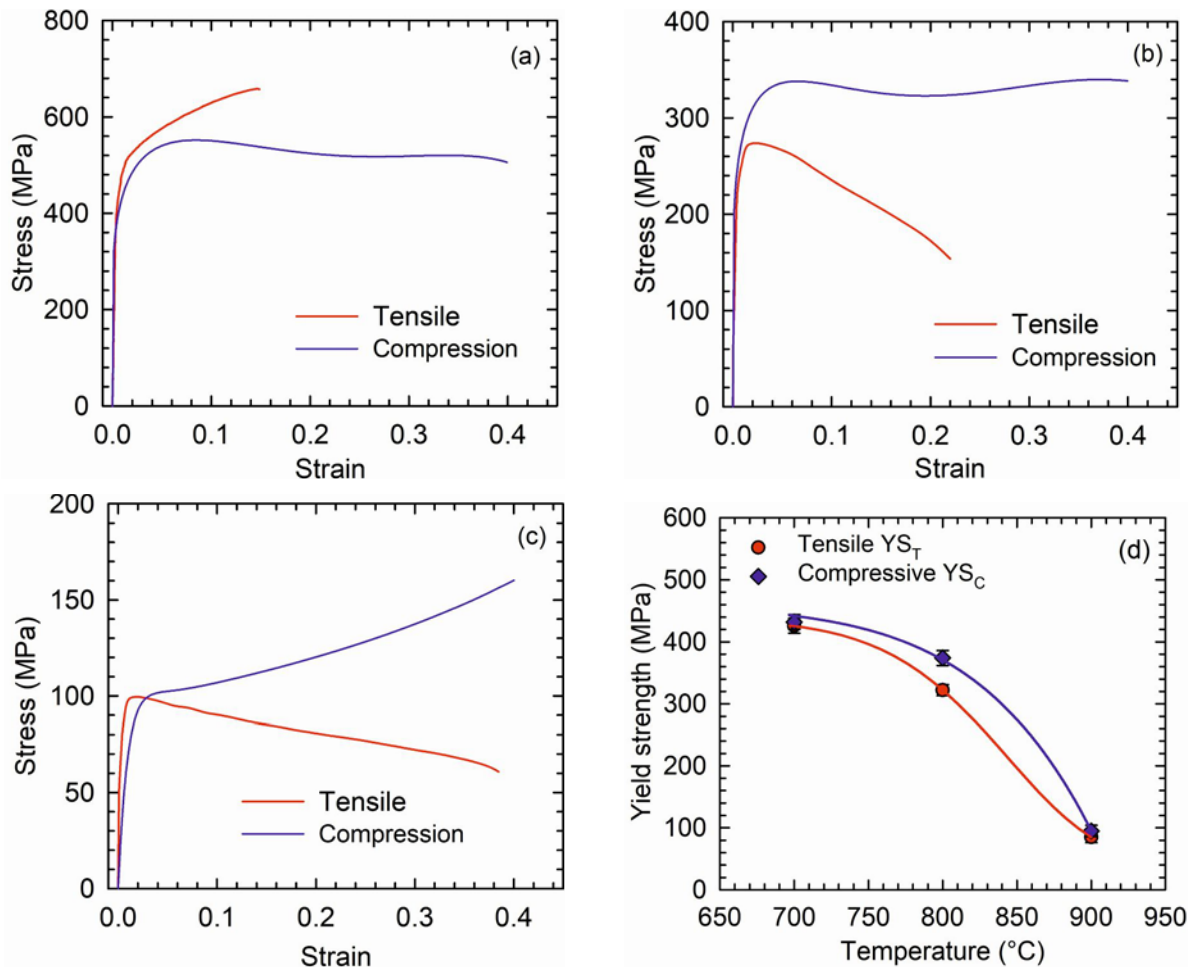


Fig. 3. Tensile and compression engineering stress-strain curves for the specimens tested at temperatures of (a) 700 °C, (b) 800 °C, (c) 900 °C, and (d) temperature dependence of average 0.2 % offset tensile and compression yield strength.

sile behaviour of multiphase CCA of a very close composition was recently published by Lapin et al. [47]. $\text{Al}_{0.5}\text{CoCr}_{1.3}\text{FeNi}_{1.3}(\text{Ti, Si, B, C})_{0.3}$ alloy prepared by directional solidification (DS) and subsequently annealed at 900 °C for 25 h was tested in tensile from 20 to 900 °C at an initial strain rate $1 \times 10^{-4} \text{ s}^{-1}$. The alloy with columnar dendrites oriented in a direction parallel or nearly parallel to the load axis composed of FCC(A1) + BCC(B2) microstructure offers YS_T 315 MPa and 185 MPa at 800 and 900 °C, respectively.

Figures 4a–c show tensile and compression true stress-true strain curves for the specimens tested at temperatures of 700, 800, and 900 °C, respectively. The tensile curve measured at 700 °C indicates only the strain hardening stage up to the fracture. The tensile deformation behaviour of the alloy changes with the increase in the test temperature over 700 °C. During 800 and 900 °C tensile, the true stress first increases to a peak value of 281 and 102 MPa with increasing true strain up to 0.034 and 0.028, respectively. Then, the alloy undergoes softening followed by true stress decrease up to a tensile fracture of the specimens.

Compressive true stress-true strain curves can be divided into two stages, i.e., the work hardening stage and the dynamic softening stage. Work hardening is observed in the alloy within small strains. During 700, 800, and 900 °C compression, the true stress first increases to a peak value of 645, 320, and 98 MPa with increasing true strain up to 0.094, 0.047, and 0.041, respectively. Then, follow the softening stage. After the peak value was reached at 900 °C tests, the dependence of the true stress and true strain is of constant flow.

3.3. Numerical simulation of tensile and compression tests

The numerical modelling of the mechanical behaviour of the alloy during high-temperature tensile and compression tests was carried out using measured data. FEA numerical calculations of experimental tensile and compression true stress-true strain curves are included in Figs. 4a–c. The FEA results are in very good agreement with the experimentally measured

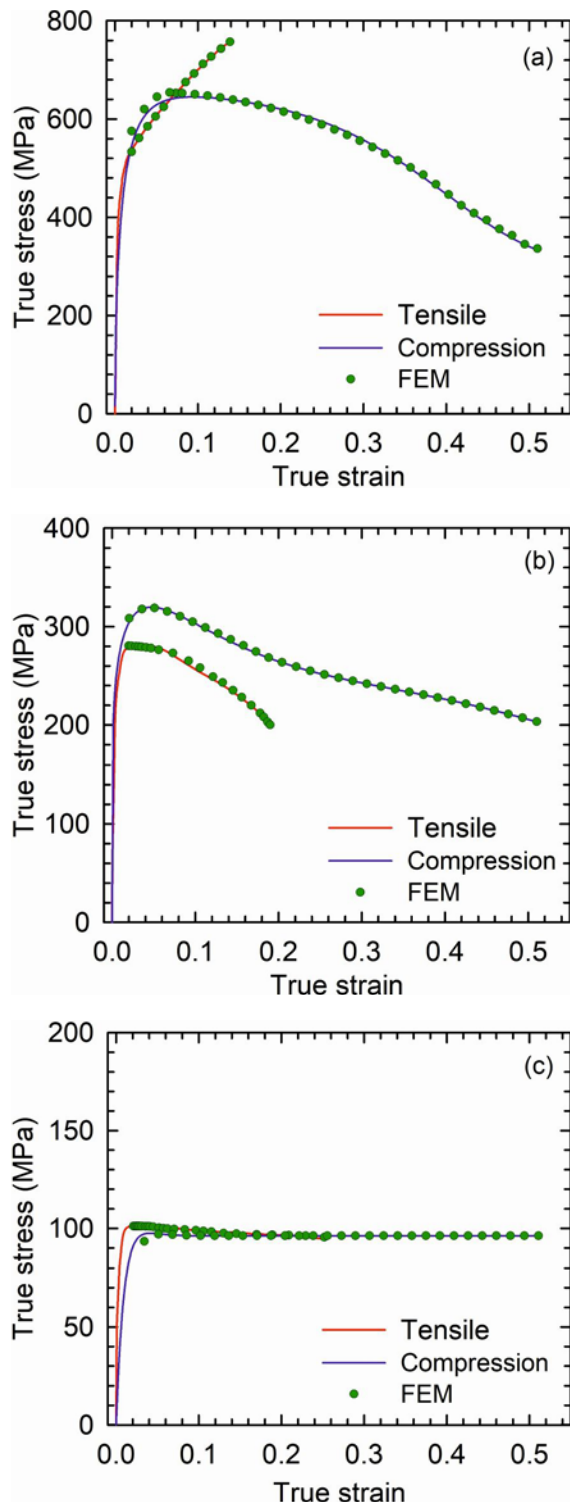


Fig. 4. Tensile and compression true stress-true strain curves with numerical simulation for the specimens tested at temperatures of (a) 700°C, (b) 800°C, and (c) 900°C.

true stress-true strain curves. Drucker-Prager softening linear model corresponds very well with experimental data.

Figures 5a–f show 3D numerical calculations of

equivalent plastic strain distribution of the tensile and compression specimens tested at temperatures of 700, 800, and 900°C to the fracture up to the true strain of 0.14, 0.19, and 0.25 for tensile tests (Figs. 5a,c,e) and to the true strain of 0.5 for compression tests (Figs. 5b,d,f). The FEA results of tensile specimens tested at 700°C indicate uniform deformation without necking. The results of tensile specimens tested at temperatures of 800 and 900°C indicate no uniform deformation with necking and achieving local maximum strains up to 0.25 in the necked region. Within the compression specimens, the equivalent plastic strain varies spatially and decreases gradually from the highest value of 2.04, 1.75, and 0.84 in the central region to 0.15, 0.13, and 0.2 in the vicinity of the specimen contact surfaces with the plates at temperatures of 700, 800, and 900°C (Figs. 5b,d,f), respectively. As we have already mentioned in the tensile and compressive curves at a temperature of 900°C, a steady-state deformation at constant flow stress occurs after reaching the peak value, which is also indicated by the shape of the specimens during the numerical simulation.

3.4. Post-deformation microstructure

3.4.1. Microstructure after tensile deformation

Figures 6a–f show the microstructure of the necked area after tensile tests at 700, 800, and 900°C in the close area of the fracture. As shown in Fig. 4, test temperature significantly influences the deformation behaviour of the alloy during tensile tests. Figure 6b shows the microstructure after tensile tests at 700°C. Various cracks were observed preferentially within Cr₂B and TiC particles and on their interfaces with other phases formed in the interdendritic region. No cracks were observed within FCC(A1) dendrites. The ductility of the alloy increases with increasing temperature, as seen at tensile curves in Figs. 3, 4, and relates to the plastic behaviour of dendrites elongated in the direction of tensile load (Figs. 6a,c,e). During tensile tests at 800°C and higher temperatures, precipitation of needle-like particles was observed in FCC(A1) dendrites. Our previous work identified these particles as ordered BCC(B2) phase [48]. Moreover, Fig. 6d shows the formation of elongated particles oriented nearly perpendicularly to the load axis in the BCC(B2)/BCC(A2) region. The same particles were found in the BCC(B2)/BCC(A2) region in as-cast Al_{0.5}CoCrFeNi alloy and identified to belong to the FCC(A1) phase [32]. More intense precipitation of ductile FCC(A1) particles in BCC(B2)/BCC(A2) region and inhomogeneous precipitation of BCC(B2) in FCC(A1) dendrite matrix occur during tensile deformation at 900°C. Formation of needle-like BCC(B2)

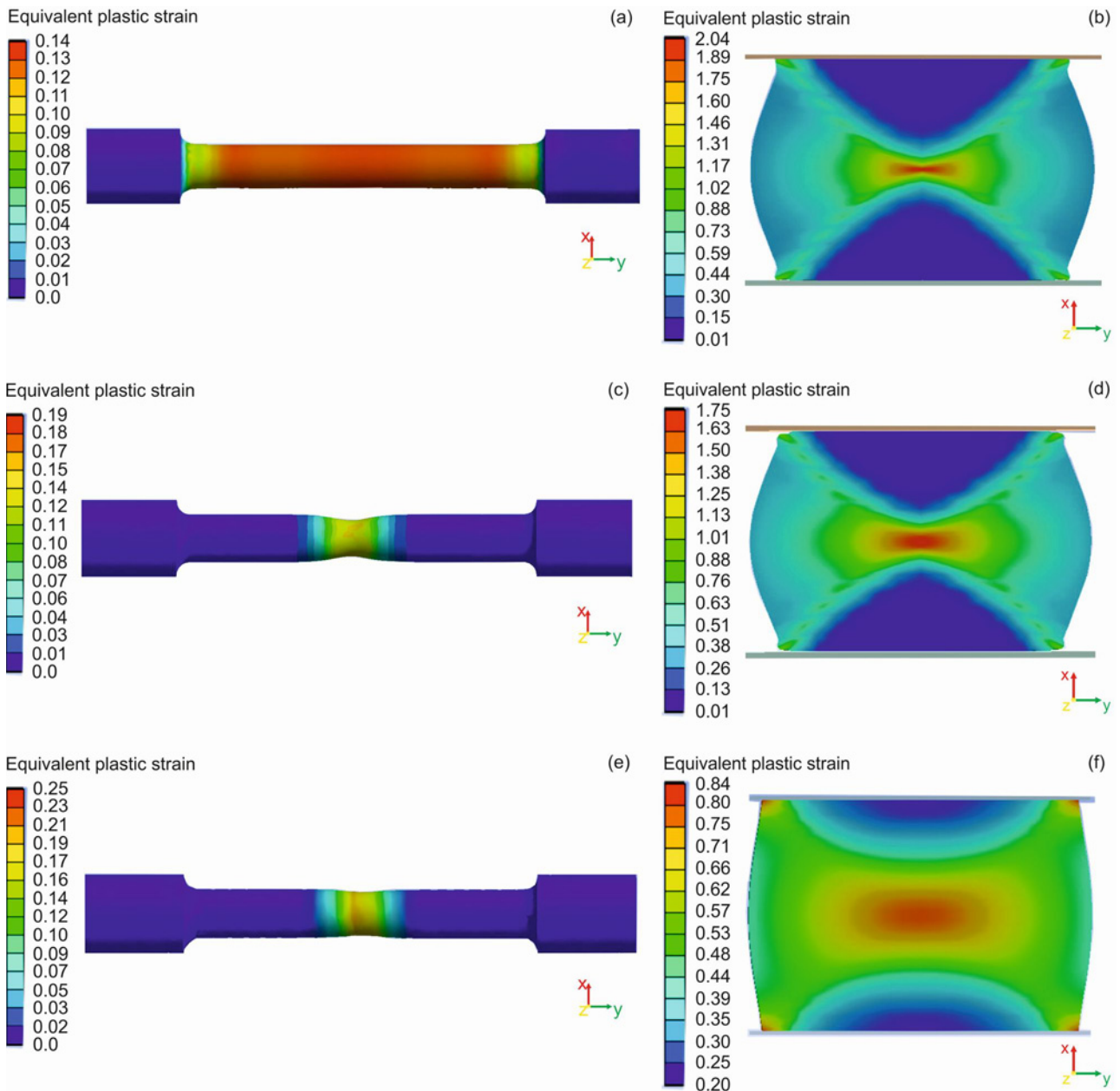


Fig. 5. FEA of equivalent plastic strains distribution in the tensile and compression specimens tested at 700, 800, and 900 °C temperatures.

precipitates due to high-temperature tensile loading within FCC(A1) matrix with composition given in Table 1 was observed recently by Lapin et al. [47] in DS $\text{Al}_{0.5}\text{CoCr}_{1.3}\text{FeNi}_{1.3}(\text{Ti, Si, B, C})_{0.3}$ alloy.

Nevertheless, regardless of the fracture pattern or test temperature, the fracture path follows the dendrite/inter-dendrite interface, as seen in Figs. 6a,c,e. High elastic modulus Cr_2B particles and TiC can be effectively loaded to stresses corresponding to their fracture strength during high-temperature tensile testing. As shown in Figs. 6b,d,f, the cracks are preferentially initiated in these high modulus phases. The tensile failure occurred by the coalescence and

propagation of the cracks and cavities formed in brittle phases and at interfaces of brittle ordered phases with FCC(A1) matrix. Temperature and strain-induced phase transformations at the temperature of 800 °C and higher contribute to the strain-hardening of the alloy; however, this contribution is not as large to compensate for the softening processes of the columnar dendrites.

3.4.2. Microstructure after compressive deformation

Figures 7a–f show the microstructure of the spec-

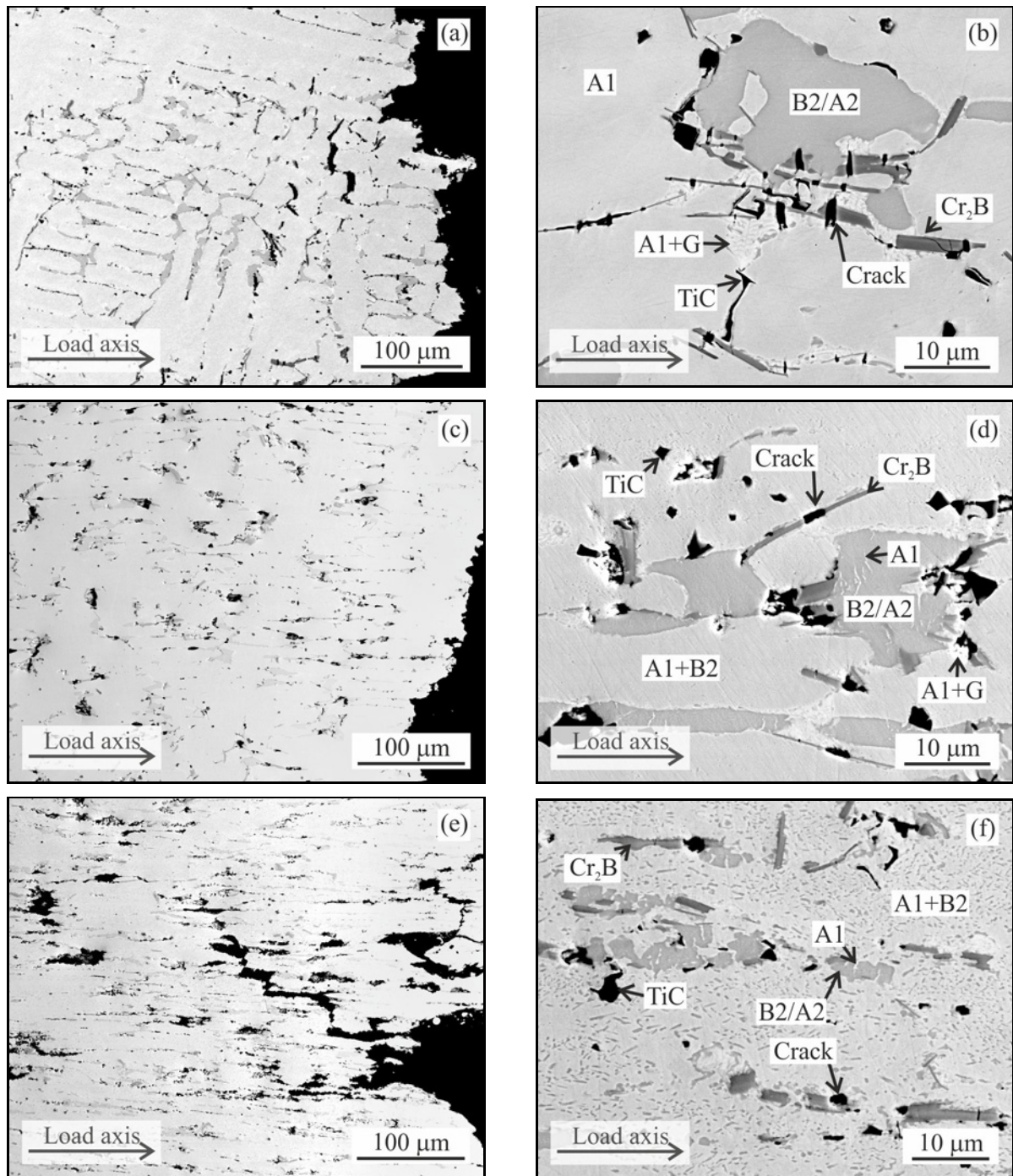


Fig. 6. BSE micrographs showing a longitudinal section of the tensile specimens in the close vicinity of the fracture surface: (a) tested at 700 °C, (b) morphology of phases of IR after 700 °C tensile, (c) tested at 800 °C, (d) morphology of phases of IR after 800 °C tensile, (e) tested at 900 °C, and (f) morphology of phases of IR after 900 °C tensile.

imens after compression tests at the strain rate of $1 \times 10^{-4} \text{ s}^{-1}$ and the temperature of 700, 800, and 900 °C, respectively. Figures 7a,c,e show the orientation of ductile dendrites and inter-dendrite region to the load axis in the central region of deformed samples, where the highest deformation operated during compression. No cracks or voids were observed in this region. Figures 7b,d,f show dynamic precipitation of

brittle BCC(B2) precipitates in ductile FCC(A1) matrix during the compression. As shown in Fig. 7f, temperature and deformation governed phase transformation of FCC(A1) \rightarrow FCC(A1) + BCC(B2) lead to inhomogeneous distribution and coarsening of BCC(B2) precipitates during 900 °C compression. Local strain conditions in the central region of the specimens lead to the bending and fragmentation of brittle elongated

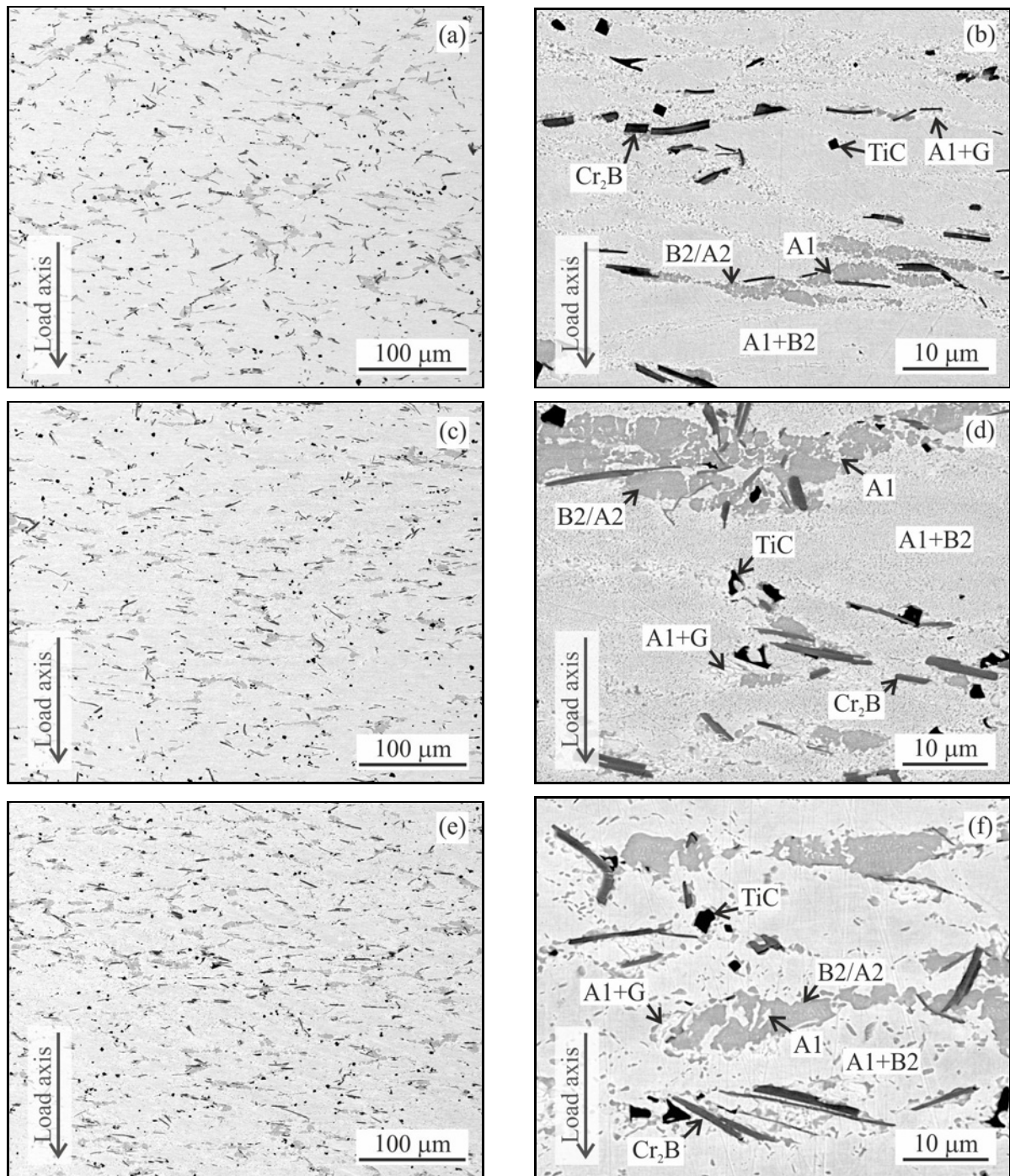


Fig. 7. BSE micrographs showing a longitudinal section of the compression specimen in the area with the highest deformation: (a) tested at 700 °C, (b) morphology of phases of IR after 700 °C compression, (c) tested at 800 °C, (d) morphology of phases of IR after 800 °C compression, (e) tested at 900 °C, and (f) morphology of phases of IR after 900 °C compression.

CrB_2 particles and to an intensive plastic deformation of the FCC(A1) + BCC(B2) matrix as well as other ductile phases like eutectic FCC(A1) + G and BCC(B2)/BCC(A2) region where intensive precipitation and deformation of ductile FCC(A1) particles occurred, as seen in Figs. 7b,d,f.

Figure 8 shows the microstructure of the barrelled region after compression tests. Nevertheless, no frac-

ture was observed at the surface of the samples during high-temperature compression at a true strain of 0.5; few cracks at the dendrite/interdendrite interfaces were formed in the vicinity of the barrelled surfaces, as seen in Figs. 8a,c,e. Figures 8b,d,f show the effect of applied temperature and local strain distributions on the morphology of intermetallic phases, phase transformations FCC(A1) \rightarrow FCC(A1) + BCC(B2)

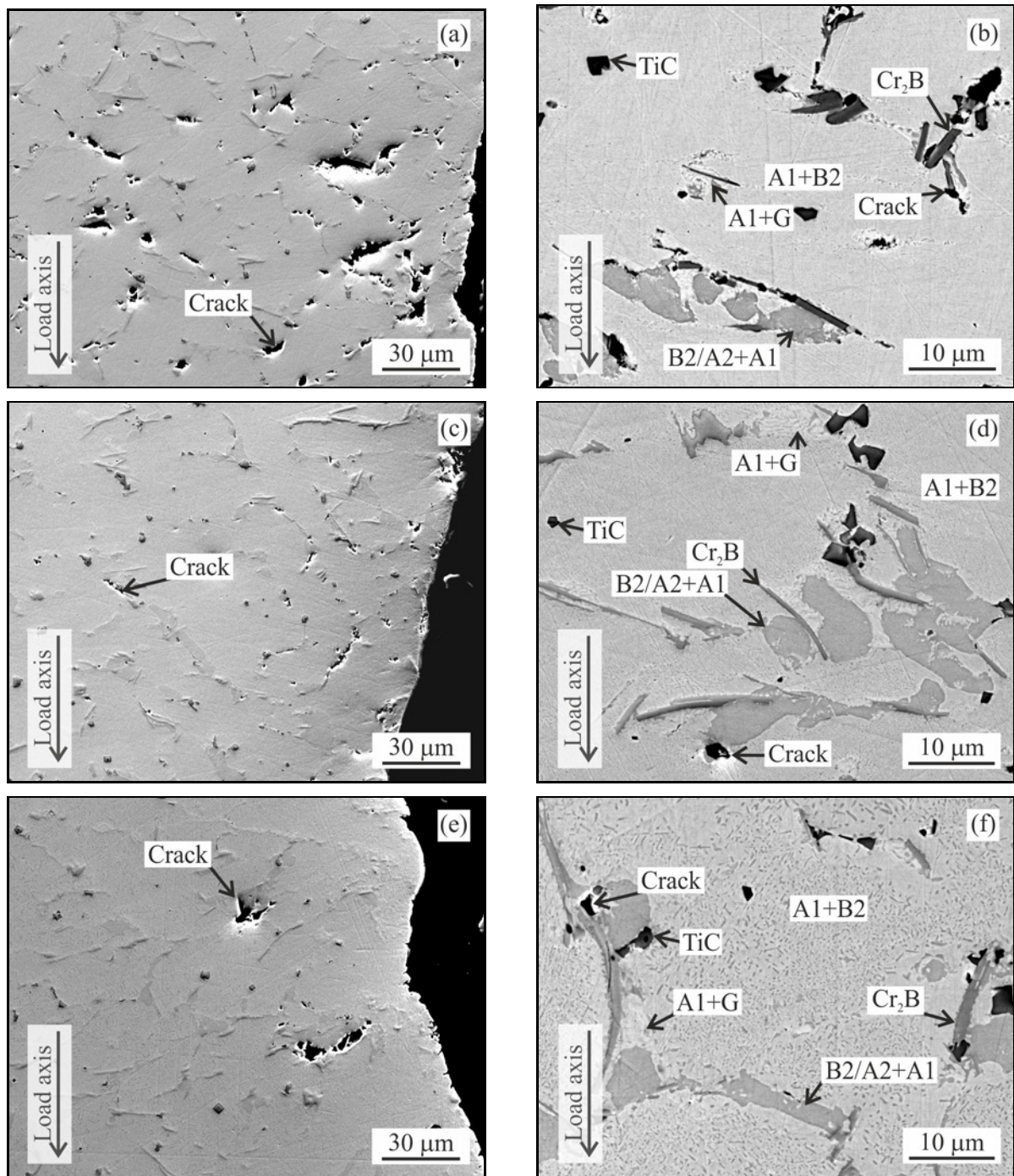


Fig. 8. The micrographs showing deformation microstructure of the compression specimen in the area of barrelled surface: (a) tested at 700 °C, SE, (b) morphology of phases of IR after 700 °C test, BSE, (c) tested at 800 °C, SE, (d) morphology of phases of IR after 800 °C test, BSE, (e) tested at 900 °C, SE, and (f) morphology of phases of IR after 900 °C test, BSE.

and $\text{BCC}(\text{B2})/\text{BCC}(\text{A2}) \rightarrow \text{BCC}(\text{B2})/\text{BCC}(\text{A2}) + \text{FCC}(\text{A1})$ as well as crack initiation near the barrelled surface. A few cracks and bending of Cr_2B particles can be observed in the alloy. Cracking decreases, and the bending of Cr_2B particles increases with the increasing temperature. In comparison with the central region where dynamic precipitation of $\text{BCC}(\text{B2})$ in the $\text{FCC}(\text{A1})$ matrix was observed at temperatures

of 700 and 800 °C, only limited $\text{BCC}(\text{B2})$ precipitation was observed in the barrelled region. Thermal-deformation conditions lead to dynamic precipitation of $\text{BCC}(\text{B2})$ in $\text{FCC}(\text{A1})$ during 900 °C compression, as seen in Fig. 8f.

Studied $\text{Al}_{0.4}\text{Co}_{0.9}\text{Cr}_{1.2}\text{Fe}_{0.9}\text{Ni}_{1.2}(\text{Si}, \text{Ti}, \text{C}, \text{B})_{0.375}$ alloy is formed by 89 vol.% of columnar dendrites and 11 vol.% of ordered phases formed in the interdendritic

region after casting [48]. The effect of the temperature and strain on the behaviour of ordered phases of the interdendritic region and the deformation behaviour of the ductile columnar FCC(A1) dendritic matrix must be considered during mechanical tests. The deformation behaviour of FCC(A1) dendrites of the studied alloy might be similar to that of $\text{Al}_{0.3}\text{CoCrFeNi}$ a high-entropy alloy composed entirely of FCC(A1) dendrite structure. As shown in Table 1, the chemical composition of FCC(A1) dendrites of the studied alloy is close to Al and comparable to Ni content as measured in $\text{Al}_{0.3}\text{CoCrFeNi}$ HEA [43]. At the beginning of the deformation, work hardening is the main mechanism in the FCC(A1) phase due to the dramatic increase in dislocation density, as observed by many authors [15, 17, 42–44]. To understand the deformation mechanism of $\text{Al}_{0.3}\text{CoCrFeNi}$ alloy, Tong et al. [44] realised compression experiments at ambient temperatures over 750°C and different strain rates, including $5 \times 10^{-4} \text{ s}^{-1}$ with a maximum height reduction of 50%. Analogous to our alloy, they observed dynamic BCC(B2) precipitation in the FCC(A1) matrix during compression. Moreover, they determined the threshold stress (σ_{th}) representing the strength of dislocation-precipitate interaction at temperatures of 750, 800, and 900°C to be 193.49, 116.07, and 32.02 MPa, respectively. This study shows that the barriers to the dislocations overcoming the precipitates are affected by temperature. Patnamsetty et al. [43] studied the compressive behaviour of $\text{Al}_{0.3}\text{CoCrFeNi}$ high-entropy alloy in temperatures of $750\text{--}1150^\circ\text{C}$ and strain rates range $10^{-3}\text{--}10 \text{ s}^{-1}$. According to the results in [43], the alloy undergoes dynamic recovery at temperatures under 850°C at the strain rate of 10^{-3} s^{-1} . Even though this strain rate is one order higher than the strain rate used at the tests of our alloy, we suppose that the same deformation mechanism but of a different value operates at the temperature of 800°C . The results of Patnamsetty et al. [22], where $\text{Al}_{0.3}\text{CoCrFeNi}$ HEA behaviour during compression at temperatures from 1030°C up to 1150°C and different strain rates, including 10^{-5} s^{-1} , was studied, imply the same conclusion. Dynamic recovery and dynamic recrystallisation of the FCC(A1) matrix are the main softening mechanisms in $\text{Al}_{0.3}\text{CoCrFeNi}$ HEA alloy [42–44].

Numerical simulations in Fig. 5 indicate that the equivalent plastic strain distribution in compression specimens varies extremely with the temperature. As seen in Fig. 4, the hardening and softening stages of the flow curves obtained at a temperature of 900°C are followed by the steady-state stage. Compression at a temperature of 900°C leads to a 58.8% decrease of equivalent plastic strain distribution in the central region and its 46.6% increase in the barrelled region compared with the 700°C sample.

The fragmentation of brittle particles like Cr_2B qualitatively corresponds to the numerical calcula-

tions of high local strains. The high local strains at a distance of 2 mm from the barrelled surface at the position corresponding to maximum diameter lead to the fragmentation of Cr-rich particles only at the test temperatures of 700 and 800°C , as seen in Figs. 7a,c. The number of fragmented particles decreases with increasing test temperature, and only limited fragmentation is observed at 900°C (Fig. 7e). These results indicate that the hot working process can be applied without degradation of brittle reinforcing phases in the studied CCA when an optimal combination of processing parameters is selected.

5. Conclusions

The deformation behaviour of as-cast $\text{Al}_{0.4}\text{Co}_{0.9}\text{Cr}_{1.2}\text{Fe}_{0.9}\text{Ni}_{1.2}(\text{Si}, \text{Ti}, \text{C}, \text{B})_{0.375}$ complex concentrated alloy (CCA) in the temperature range from 700 up to 900°C during tensile and compression tests was studied. The achieved results can be summarised as follows:

- The initial microstructure of the studied alloy is highly anisotropic and consists of columnar FCC(A1) dendrites (89 vol.%) oriented at an angle ranging from 60° to 90° to the longitudinal axis of specimens and multiphase interdendritic region (11 vol.%).

- The alloy during tensile deformation at 700°C shows the strain hardening stage up to fracture. The tensile deformation true strain-true stress curves at 800°C and compression deformation true strain-true stress curves at temperatures from 700 to 800°C show the strain hardening stage at initial strains. After reaching the peak values, the strain softening stage is typical for the alloy. The compression curves at 900°C show a short strain hardening stage, followed by a steady-state deformation at a constant flow stress.

- The increase in the test temperature from 700 to 900°C is connected with a significant decrease in the peak true stress from 755 to 102 MPa in tensile and from 645 to 98 MPa in compression and a decrease in a true strain to a peak value from 0.094 to 0.028 in tensile and from 0.138 to 0.041 in compression.

- At high temperatures, ductile fracture mode results from the growth and coalescence of voids initiated preferentially at the phase interfaces in the interdendritic region and crack propagation along the dendrite/interdendritic interfaces connected with intensive plastic deformation of FCC(A1) dendrites.

Acknowledgements

This work was financially supported by the Slovak Research and Development Agency under the contracts APVV-20-0505 and the Slovak Grant Agency for Science under VEGA 2/0018/22. The authors thank Soňa

Kružlíková for technical assistance and metallographic preparation of the samples.

References

- [1] B. Cantor, I. T. H. Chang, P. Knight, A. J. B. Vincent, Microstructural development in equiatomic multicomponent alloys, *Mater. Sci. Eng. A* 375–377 (2004) 213–218. <https://doi.org/10.1016/j.msea.2003.10.257>
- [2] B. Cantor, Multicomponent high-entropy Cantor alloys, *Prog. Mater. Sci.* 120 (2021) 100754. <https://doi.org/10.1016/j.pmatsci.2020.100754>
- [3] J. W. Yeh, S. K. Chen, J. Y. Gan, S. J. Lin, T. S. Chin, T. T. Shun, Ch. H. Tsau, S. Y. Chang, Formation of simple crystal structures in Cu-Co-Ni-Cr-Al-Fe-Ti-V alloys with multiprincipal metallic elements, *Metall. Mater. Trans.* 35 (2010) 2533–2536. <https://doi.org/10.1007/s11661-006-0234-4>
- [4] D. B. Miracle, O. N. Senkov, A critical review of high entropy alloys and related concepts, *Acta Mater.* 122 (2017) 448–511. <https://doi.org/10.1016/j.actamat.2016.08.081>
- [5] E. P. George, W. A. Curtin, C. C. Tasan, High entropy alloys: A focused review of mechanical properties and deformation mechanisms, *Acta Mater.* 188 (2020) 435–474. <https://doi.org/10.1016/j.actamat.2019.12.015>
- [6] H. Mao, H. L. Chen, Q. Chen, TCHEA1: A thermodynamic database not limited for high entropy alloys, *J. Phase Equilibria Diffus.* 38 (2017) 353–368. <https://doi.org/10.1007/s11669-017-0570-7>
- [7] D. Miracle, B. Majumdar, K. Wertz, S. Gorsse, New strategies and tests to accelerate discovery and development of multi-principal element structural alloys, *Scr. Mater.* 127 (2017) 195–200. <https://doi.org/10.1016/j.scriptamat.2016.08.001>
- [8] S. Gorsse, D. B. Miracle, O. N. Senkov, Mapping the world of complex concentrated alloys, *Acta Mater.* 135 (2017) 177–187. <https://doi.org/10.1016/j.actamat.2017.06.027>
- [9] D. B. Miracle, J. D. Miller, O. N. Senkov, C. Woodward, M. D. Uchic, J. Tiley, Exploration and development of high entropy alloys for structural applications, *Entropy* 16 (2014) 494–525. <https://doi.org/10.3390/e16010494>
- [10] Y. Zeng, M. Man, K. Bai, Y. W. Zhang, Explore the full temperature-composition space of 20 quinary CCAs for FCC and BCC single-phases by an iterative machine learning + CALPHAD method, *Acta Mater.* 231 (2022) 117865. <https://doi.org/10.1016/j.actamat.2022.117865>
- [11] A. Asabre, A. Kostka, O. Stryzhyboroda, J. Pftzting-Micklich, U. Hecht, G. Laplanche, Effect of Al, Ti and C additions on Widmanstätten microstructures and mechanical properties of cast Al_{0.6}CoCrFeNi compositionally complex alloys, *Mater. Des.* 184 (2019) 108201. <https://doi.org/10.1016/j.matdes.2019.108201>
- [12] H. Y. Diao, R. Feng, K. A. Dahmen, P. K. Liaw, Fundamental deformation behavior in high-entropy alloys: An overview, *Curr. Opin. Solid State Mater. Sci.* 21 (2017) 252–266. <https://doi.org/10.1016/j.cossms.2017.08.003>
- [13] J. Zhang, H. Qiu, H. Zhu, Z. Xie, Effect of Al additions on the microstructures and tensile properties of Al_xCoCr₃Fe₅Ni high entropy alloys, *Mater. Charact.* 175 (2021) 111091. <https://doi.org/10.1016/j.matchar.2021.111091>
- [14] M. Slobodyan, E. Pesterev, A. Markov, Recent advances and outstanding challenges for implementation of high entropy alloys as structural materials, *Mater. Today Commun.* 36 (2023) 106422. <https://doi.org/10.1016/j.mtcomm.2023.106422>
- [15] J. Li, H. Yang, W. Y. Wang, H. Kou, J. Wang, Thermal-mechanical processing and strengthen in Al_xCoCrFeNi high-entropy alloys, *Front. Mater.* 7 (2021) 585602. <https://doi.org/10.3389/fmats.2020.585602>
- [16] B. Gwalani, S. Gorsse, D. Choudhuri, Y. Zheng, R. S. Mishra, R. Banerjee, Tensile yield strength of a single bulk Al_{0.3}CoCrFeNi high entropy alloy can be tuned from 160 MPa to 1800 MPa, *Scr. Mater.* 162 (2019) 18–23. <https://doi.org/10.1016/j.scriptamat.2018.10.023>
- [17] J. Joseph, N. Stanford, P. Hodgson, D. M. Fabijanic, Understanding the mechanical behaviour and the large strength/ductility differences between FCC and BCC Al_xCoCrFeNi high entropy alloys, *J. Alloys Compd.* 726 (2017) 885–895. <https://doi.org/10.1016/j.jallcom.2017.08.067>
- [18] Y. Lv, R. Hu, Z. Yao, J. Chen, D. Xu, Y. Liu, X. Fan, Cooling rate effect on microstructure and mechanical properties of Al_xCoCrFeNi high entropy alloys, *Mater. Des.* 132 (2017) 392–399. <https://doi.org/10.1016/j.matdes.2017.07.008>
- [19] J. C. Rao, H. Y. Diao, V. Ocelík, D. Vainchtein, C. Zhang, C. Kuo, Z. Tang, W. Guo, J. D. Poplawsky, Y. Zhou, P. K. Liaw, J. Th. M. De Hosson, Secondary phases in Al_xCoCrFeNi high-entropy alloys: An in-situ TEM heating study and thermodynamic appraisal, *Acta Mater.* 131 (2017) 206–220. <https://doi.org/10.1016/j.actamat.2017.03.066>
- [20] Y. F. Kao, T. J. Chen, S. K. Chen, J. W. Yeh, Microstructure and mechanical property of as-cast, -homogenized, and -deformed Al_xCoCrFeNi (0 ≤ x ≤ 2) high-entropy alloys, *J. Alloys Compd.* 488 (2009) 57–64. <https://doi.org/10.1016/j.jallcom.2009.08.090>
- [21] W. R. Wang, W. L. Wang, S. C. Wang, Y. C. Tsai, C. H. Lai, J. W. Yeh, Effects of Al addition on the microstructure and mechanical property of Al_xCoCrFeNi high-entropy alloys, *Intermetallics* 26 (2012) 44–51. <https://doi.org/10.1016/j.intermet.2012.03.005>
- [22] M. Patnamsetty, S. Ghosh, M. C. Somani, P. Peura, Dynamic softening kinetics of Al_{0.3}CoCrFeNi high-entropy alloy during high temperature compression and its correlation with the evolving microstructure and micro-texture, *Mater. Charact.* 197 (2023) 112693. <https://doi.org/10.1016/j.matchar.2023.112693>
- [23] N. Haghdadi, S. Primig, M. Annasamy, P. Cizek, P. D. Hodgson, D. M. Fabijanic, On the hot-worked microstructure of a face-centered cubic Al_{0.3}CoCrFeNi high entropy alloy, *Scr. Mater.* 178 (2020) 144–149. <https://doi.org/10.1016/j.scriptamat.2019.11.022>
- [24] B. Gwalani, S. Gorsse, D. Choudhuri, M. Styles, Y. Zheng, R. S. Mishra, R. Banerjee, Modifying transformation pathways in high entropy alloys or complex concentrated alloys via thermo-mechanical processing, *Acta Mater.* 153 (2018) 169–185. <https://doi.org/10.1016/j.actamat.2018.05.009>

- [25] M. Annasamy, N. Haghdam, A. Taylor, P. Hodgson, D. Fabijanic, Dynamic recrystallization behaviour of $\text{Al}_x\text{CoCrFeNi}$ high entropy alloys during high-temperature plane strain compression, *Mater. Sci. Eng. A* 745 (2019) 90–106. <https://doi.org/10.1016/j.msea.2018.12.102>
- [26] J. Jiang, W. Sun, N. Luo, Molecular dynamics study of microscopic deformation mechanism and tensile properties in $\text{Al}_x\text{CoCrFeNi}$ amorphous high-entropy alloys, *Mater. Today Commun.* 31 (2022) 103861. <https://doi.org/10.1016/j.mtcomm.2022.103861>
- [27] Q. Chen, Y. Dong, J. Zhang, Y. Lu, Microstructure and properties of AlCoCrFeNiB_x ($x = 0, 0.1, 0.25, 0.5, 0.75, 1.0$) high entropy alloys, *Rare Met. Mater. Eng.* 46 (2017) 651–656. [https://doi.org/10.1016/s1875-5372\(17\)30112-1](https://doi.org/10.1016/s1875-5372(17)30112-1)
- [28] B. Gwalani, D. Choudhuri, K. Liu, J. T. Lloyd, R. S. Mishra, R. Banerjee, Interplay between single phase solid solution strengthening and multi-phase strengthening in the same high entropy alloy, *Mater. Sci. Eng. A* 771 (2020) 138620. <https://doi.org/10.1016/j.msea.2019.138620>
- [29] Z. Tang, O. N. Senkov, C. M. Parish, C. Zhang, F. Zhang, L. J. Santodonato, G. Wang, G. Zhao, F. Yang, P. K. Liaw, Tensile ductility of an AlCoCrFeNi multiphase high-entropy alloy through hot isostatic pressing (HIP) and homogenization, *Mater. Sci. Eng. A* 647 (2015) 229–240. <https://doi.org/10.1016/j.msea.2015.08.078>
- [30] M. Aizenshtein, E. Priel, S. Hayun, Effect of pre-deformation and B2 morphology on the mechanical properties of $\text{Al}_{0.5}\text{CoCrFeNi}$ HEA, *Mater. Sci. Eng. A* 788 (2020) 139575. <https://doi.org/10.1016/j.msea.2020.139575>
- [31] M. Štamborská, J. Lapin, Effect of anisotropic microstructure on high-temperature compression deformation of CoCrFeNi based complex concentrated alloy, *Kovove Mater.* 55 (2017) 369–378. https://doi.org/10.4149/km-2017_6-369
- [32] J. Lapin, M. Makwana, A. Klimová, Effect of heat treatments on microstructure and mechanical properties of $\text{Al}_{0.5}\text{CoCrFeNi}$ complex concentrated alloy, *Kovove Mater.* 59 (2021) 79–91. https://doi.org/10.4149/km-2021_2-79
- [33] V. Ferrari, W. Wolf, G. Zepon, F. G. Coury, M. J. Kaufman, C. Bolfarini, C. S. Kiminami, W. J. Botta, Effect of boron addition on the solidification sequence and microstructure of AlCoCrFeNi alloys, *J. Alloys Compd.* 775 (2019) 1235–1243. <https://doi.org/10.1016/j.jallcom.2018.10.268>
- [34] J. M. Zhu, H. M. Fu, H. F. Zhang, A. M. Wang, H. Li, Z. Q. Hu, Synthesis and properties of multiprincipal component AlCoCrFeNiSi_x alloys, *Mater. Sci. Eng. A* 527, 27–28 (2010) 7210–7214. <https://doi.org/10.1016/j.msea.2010.07.049>
- [35] Q. S. Chen, Y. P. Lu, Y. Dong, T. M. Wang, T. J. Li, Effect of minor B addition on microstructure and properties of AlCoCrFeNi multi-component alloy, *Trans. Nonferrous Met. Soc. China* 25 (2015) 2958–2964. [https://doi.org/10.1016/S1003-6326\(15\)63922-X](https://doi.org/10.1016/S1003-6326(15)63922-X)
- [36] J. M. Zhu, H. M. Fu, H. F. Zhang, A. M. Wang, H. Li, Z. Q. Hu, Microstructure and compressive properties of multiprincipal component AlCoCrFeNiC_x alloys, *J. Alloys Compd.* 509 (2011) 3476–3480. <https://doi.org/10.1016/j.jallcom.2010.10.047>
- [37] L. J. Zhang, P. F. Yu, J. T. Fan, M. D. Zhang, C. Z. Zhang, H. Z. Cui, G. Li, Investigating the micro and nanomechanical properties of CoCrFeNi-C_x high-entropy alloys containing eutectic carbides, *Mater. Sci. Eng. A* 796 (2020) 140065. <https://doi.org/10.1016/j.msea.2020.140065>
- [38] M. C. Oh, A. Sharma, H. Lee, B. Ahn, Phase separation and mechanical behavior of AlCoCrFeNi-X ($X = \text{Cu, Mn, Ti}$) high entropy alloys processed via powder metallurgy, *Intermetallics* 139 (2021) 107369. <https://doi.org/10.1016/j.intermet.2021.107369>
- [39] S. Jiang, Z. Lin, H. Xu, Y. Sun, Studies on the microstructure and properties of $\text{Al}_x\text{CoCrFeNiTi}_{1-x}$ high entropy alloys, *J. Alloys Compd.* 741 (2018) 826–833. <https://doi.org/10.1016/j.jallcom.2018.01.247>
- [40] P. Cheng, Y. Zhao, X. Xu, S. Wang, Y. Sun, H. Hou, Microstructural evolution and mechanical properties of $\text{Al}_{0.3}\text{CoCrFeNiSi}_x$ high-entropy alloys containing coherent nanometer-scaled precipitates, *Mater. Sci. Eng. A* 772 (2020) 138681. <https://doi.org/10.1016/j.msea.2019.138681>
- [41] X. Gu, Y. Zhuang, P. Jia, Evolution of phase, microstructure and mechanical properties of as-cast $\text{Al}_{0.3}\text{CoCrFeNiTi}_x$ high entropy alloys, *Mater. Today Commun.* 31 (2022) 103328. <https://doi.org/10.1016/j.mtcomm.2022.103328>
- [42] W. J. Kim, H. T. Jeong, H. K. Park, K. Park, T. W. Na, E. Choi, The effect of Al to high-temperature deformation mechanisms and processing maps of $\text{Al}_{0.5}\text{CoCrFeMnNi}$ high entropy alloy, *J. Alloys Compd.* 802 (2019) 152–165. <https://doi.org/10.1016/j.jallcom.2019.06.099>
- [43] M. Patnamsetty, S. Ghosh, M. C. Somani, P. Peura, Characterization of hot deformation behavior of $\text{Al}_{0.3}\text{CoCrFeNi}$ high-entropy alloy and development of processing map, *J. Alloys Compd.* 914 (2022) 165341. <https://doi.org/10.1016/j.jallcom.2022.165341>
- [44] Y. Tong, J. C. Qiao, Y. Yao, The constitutive model and threshold stress for characterizing the deformation mechanism of $\text{Al}_{0.3}\text{CoCrFeNi}$ high entropy alloy, *Mater. Sci. Eng. A* 730 (2018) 137–146. <https://doi.org/10.1016/j.msea.2018.05.109>
- [45] D. Chen, F. He, B. Han, Q. Wu, Y. Tong, Y. Zhao, Z. Wang, J. Wang, J. J. Kai, Synergistic effect of Ti and Al on L12-phase design in CoCrFeNi -based high entropy alloys, *Intermetallics* 110 (2019) 106476. <https://doi.org/10.1016/j.intermet.2019.106476>
- [46] M. H. Tsai, R. C. Tsai, T. Chang, W. F. Huang, Intermetallic phases in high-entropy alloys: Statistical analysis of their prevalence and structural inheritance, *Metals* 9 (2019) 247. <https://doi.org/10.3390/met9020247>
- [47] J. Lapin, A. Klimová, T. Pelachová, O. Bajana, Microstructure evolution and mechanical properties of directionally solidified $\text{Al}_{0.5}\text{CoCr}_{1.3}\text{FeNi}_{1.3}(\text{Ti, Si, B, C})_{0.3}$ multiphase complex concentrated alloy, *Intermetallics* 162 (2023) 108033. <https://doi.org/10.1016/j.intermet.2023.108033>
- [48] J. Lapin, A. Klimová, T. Pelachová, M. Štamborská, O. Bajana, Synergistic effect of Ti, B, Si, and C on microstructure and mechanical properties of as-cast $\text{Al}_{0.4}\text{Co}_{0.9}\text{Cr}_{1.2}\text{Fe}_{0.9}\text{Ni}_{1.2}(\text{Si, Ti, C, B})_{0.375}$ complex concentrated alloy, *J. Alloys Compd.* 934 (2022)

168050.
<https://doi.org/10.1016/j.jallcom.2022.168050>
- [49] K. K. Alaneme, M. O. Bodunrin, S. R. Oke, Processing, alloy composition and phase transition effect on the mechanical and corrosion properties of high entropy alloys: A review, *J. Mater. Res. Technol.* 5 (2016) 384–393.
<https://doi.org/10.1016/j.jmrt.2016.03.004>
- [50] P. Berthod, As-cast microstructures of high entropy alloys designed to be TaC-strengthened, *J. Met. Mater. Res.* 5 (2022) 1–10.
<https://doi.org/10.30564/jmmr.v5i2.4685>
- [51] P. Kumar, S. J. Kim, Q. Yu, J. Ell, M. Zhang, Y. Yang, J. Y. Kim, H. K. Park, A. M. Minor, E. S. Park, R. O. Ritchie, Compressive vs. tensile yield and fracture toughness behavior of a body-centered cubic refractory high-entropy superalloy Al_{0.5}Nb_{1.25}Ta_{1.25}TiZr at temperatures from ambient to 1200 °C, *Acta Mater.* 245 (2023) 118620.
<https://doi.org/10.1016/j.actamat.2022.118620>
- [52] J. Joseph, N. Stanford, P. Hodgson, D. M. Fabijanic, Tension/compression asymmetry in additive manufactured face centered cubic high entropy alloy, *Scr. Mater.* 129 (2017) 30–34.
<https://doi.org/10.1016/j.scriptamat.2016.10.023>
- [53] Y. Qi, M. Zhao, M. Feng, Molecular simulation of microstructure evolution and plastic deformation of nanocrystalline CoCrFeMnNi high-entropy alloy under tension and compression, *J. Alloys Compd.* 851 (2021) 156923.
<https://doi.org/10.1016/j.jallcom.2020.156923>
- [54] M. Štamborská, J. Lapin, O. Bajana, M. Losertová, Tensile deformation behaviour of ferritic-pearlitic steel studied by digital image correlation method, *Kovove Mater.* 53 (2015) 399–407.
<https://doi.org/10.4149/km-2015-6-399>
- [55] M. Štamborská, J. Lapin, O. Bajana, Effect of hydrogenation on deformation behaviour of ferritic-pearlitic steel studied by digital image correlation method, *Kovove Mater.* 54 (2016) 397–406.
<https://doi.org/10.4149/km-2016-6-397>
- [56] M. Štamborská, M. Losertová, K. Konečná, V. Mareš, L. Horsák, Comparative strain analysis of 34CrMo4 steel and Inconel 738LC, *Kovove Mater.* 53 (2015) 305–311. <https://doi.org/10.4149/km-2015-5-305>
- [57] M. Štamborská, J. Lapin, K. Kamysnykova, Preparation, microstructure, and mechanical behaviour of Ni₃Al-based superalloy reinforced with carbide particles, *Intermetallics* 149 (2022) 107667.
<https://doi.org/10.1016/j.intermet.2022.107667>